

See discussions, stats, and author profiles for this publication at: <https://www.researchgate.net/publication/373515729>

# Capacity prediction and design optimization for laterally loaded monopiles in sandy soil using hybrid neural network and sequential quadratic programming

Article in *Computers and Geotechnics* · November 2023

DOI: 10.1016/j.compgeo.2023.105745

CITATIONS

0

READS

51

3 authors, including:



Amir Hosein Taherkhani  
University of New Hampshire

4 PUBLICATIONS 21 CITATIONS

SEE PROFILE



Fei Han  
University of New Hampshire

37 PUBLICATIONS 721 CITATIONS

SEE PROFILE

1 **Capacity prediction and design optimization for laterally loaded monopiles**  
2 **in sandy soil using hybrid neural network and sequential quadratic**  
3 **programming**

4  
5 Amir Hosein Taherkhani<sup>1</sup>, Qipei Mei<sup>2</sup>, Fei Han<sup>1</sup>  
6

7 <sup>1</sup>Department of Civil and Environmental Engineering, University of New Hampshire, Durham, NH,  
8 USA

9 <sup>2</sup>Faculty of Engineering - Civil and Environmental Engineering Dept, University of Alberta, Edmonton,  
10 AB, Canada  
11

12 **ABSTRACT**

13 Data driven methods have gained momentum in recent years in solving highly non-  
14 linear engineering problems that are challenging to solve using conventional methods. In this  
15 paper, we present a hybrid neural network model to predict the lateral response of large-  
16 diameter monopiles in multi-layered soil. The hybrid neural network consists of a mixture of  
17 convolutional and fully-connected layers, which capture the impacts of the soil profile, the pile  
18 geometry, and loading conditions on the lateral load response of monopiles. To train the neural  
19 network model, we produced data from high-fidelity three-dimensional (3D) finite element (FE)  
20 models that are validated against full-scale pile load tests. To ensure consistent model  
21 performance across the entire range of pile capacities considered in the dataset (ranging from  
22 approximately 100 kN to 100,000 kN), we utilize the relative error (percentage error) as the  
23 criterion for training the model. To achieve this goal, we explored six different combinations  
24 of data transformation methods (i.e., natural logarithm and root transformations) and cost  
25 functions. Among these models, the model trained with Mean Squared Error (MSE) using  
26 natural logarithm transformation yielded the most accurate and consistent predictions of the  
27 lateral capacities of monopiles. To demonstrate the strengths of the developed neural network  
28 model, it was used as a surrogate model to perform pile design optimization using sequential

29 quadratic programming. In addition, a design example is provided to show how the developed  
30 method can be easily implemented.

## 31 **1 INTRODUCTION**

32 The offshore wind industry has grown exponentially in the last decade driven by the  
33 increasing demand for clean renewable energy. Large-scale offshore wind turbines are often  
34 supported on monopiles, a foundation type that is made of a single open-ended steel pipe driven  
35 or jacked into the seabed. The lateral load design for these large-diameter monopiles has  
36 traditionally relied on the  $p$ - $y$  method. This method considers the pile as a one-dimensional  
37 Euler-Bernoulli beam while the soil medium is modeled as a series of non-linear springs  
38 attached to the beam. Since this method was originally developed and used for slender pile  
39 design, its applicability for large-diameter monopiles is not well established (Doherty and  
40 Gavin 2012; Farahani et al. 2022; Suryasentana and Lehane 2016). Evidence has shown that  
41 the  $p$ - $y$  method may result in inaccurate predictions for the lateral response of monopiles (Han  
42 et al. 2015, 2017; Suryasentana and Lehane 2016).

43 In order to improve the design for large-diameter monopiles, researchers have  
44 developed new design approaches for monopiles based on three-dimensional finite-element  
45 (3D FE) analyses. When compared with the  $p$ - $y$  method, a 3D FE analysis can fully capture  
46 the 3D pile-soil interactions when a pile is laterally loaded, producing more accurate capacity  
47 predictions. 3D FE analysis has been widely used to study the lateral load response of single  
48 piles (Ahmadi and Ahmari 2009; Brown and Shie 1990; Chatterjee et al. 2015; Cheng et al.  
49 2021; Kementzetzidis et al. 2018; Murphy et al. 2018; Peng et al. 2010). Recently, Byrne et al.  
50 (2020) conducted a series of 3D FE analyses for monopiles placed in stiff and overconsolidated

51 clay, based on which the updated  $p$ - $y$  method was proposed. Taborda et al. (2020) conducted  
52 a 3D FE analysis for laterally loaded monopiles placed in dense sands, accounting for a  
53 constitutive model that captures the behavior of sand with a range of relative densities. Despite  
54 its accurate results, 3D FE analysis is computationally costly, often taking several days to  
55 complete a full-scale FE simulation (Han et al. 2015; Xu et al. 2013). In addition, the accuracy  
56 of the FE analysis is highly dependent on the knowledge and experience of the modeler. Proper  
57 meshing and selection of an appropriate constitutive model for the soil are both critical to  
58 ensure the quality of 3D FE analyses.

59 Unlike physics-based models (e.g., FE analyses), which are constructed based on  
60 physics laws and appropriate assumptions, Artificial Neural Network (ANN) models are  
61 developed to recognize the underlying patterns within the data collected for the problem of  
62 interest (Shahin 2016). When properly trained, ANN models can produce fast predictions  
63 (taking split-second computational time) with high accuracies. Inspired by the biological neural  
64 network, ANN was initially developed for simulating neurological networks in the 1940s  
65 (McCulloch and Pitts 1943). In recent years, ANN has gained popularity in solving complex  
66 geotechnical engineering problems due to the rapidly growing computational capacity and data  
67 availability (Chan and Low 2012; Huang et al. 2022; Kordjazi et al. 2014; Makasis et al. 2018;  
68 Moeinifard et al. 2022). For instance, Pham et al. (2020) and Kardani et al. (2020) developed  
69 ANN models to estimate the axial bearing capacity of driven piles. Xiao et al. (2022) developed  
70 a machine-learning based spatio-temporal forecasting model to predict landslide locations and  
71 consequences. Zhang et al. (2022) used convolutional neural network (CNN) to characterize  
72 the soil spatial variability from limited cone penetration test (CPT) data. Lai et al. (2022)  
73 developed an ANN-based framework to detect particle contacts for discrete element method

74 (DEM). ANN has been demonstrated through these studies to be a promising instrument for  
75 solving geotechnical engineering challenges.

76 In this paper, we developed an ANN model to predict the lateral load response of  
77 monopiles installed in multi-layered sandy soil. The model takes pile geometries, loading  
78 conditions, and the cone penetration test (CPT) data as inputs, generating predictions for the  
79 lateral pile capacities corresponding to different pile rotation levels at the mudline. We  
80 investigated the effectiveness of various data transformation techniques and cost functions in  
81 reducing the skewness of training datasets and improving model performance. In addition, the  
82 developed model was used as a surrogate model to perform pile design optimization.

## 83 **2 METHODOLOGY**

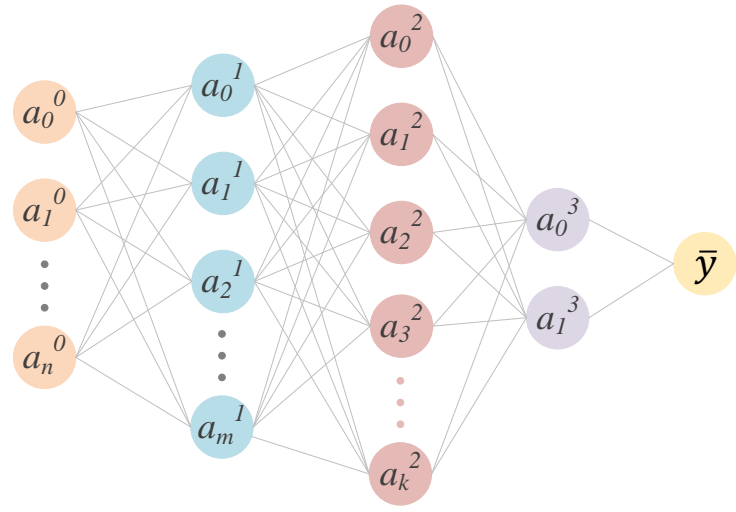
84 In this section, we first briefly explain the fundamental ideas of fully-connected (FC)  
85 neural work and convolutional neural network (CNN). Based on these two ANN methods, we  
86 propose the hybrid neural network architecture designed for this study.

### 87 **2.1. Hybrid Neural Network**

88 Deep neural network or Deep Learning (DL) is an ANN model with a structure of more  
89 than three layers (Patterson and Gibson 2017). Fully-connected (FC) neural network, also  
90 known as feed-forward neural network, is the simplest yet most widely-used type of DL. FC  
91 neural networks are often used for feature extraction for non-sequential data. As shown in  
92 Figure 1a, a FC neural network is composed of an input layer, several hidden middle layers,  
93 and an output layer. Each layer contains one or multiple nodes (also known as artificial  
94 neurons), the most fundamental units in an FC neural network. Resembling the function of

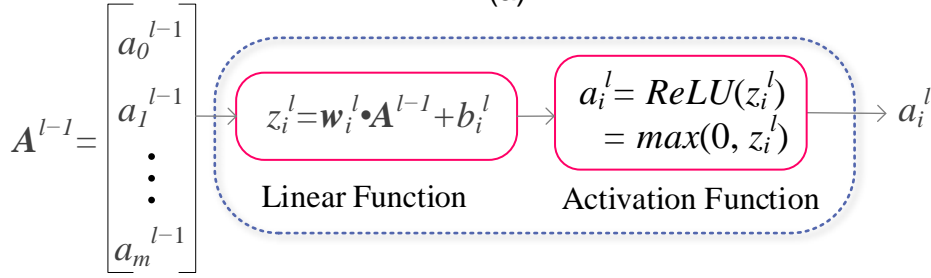
95 biological neurons, nodes are designed to process the information received from upstream  
96 nodes and then pass the processed information to the downstream nodes. To achieve this goal,  
97 a node first uses a linear function to map the outputs of all nodes from the previous layer into  
98 a single value, which is then passed into a non-linear activation function to generate the output  
99 for this node (Figure 1b). The output values for all nodes in a layer are then used as the input  
100 for the next layer. The non-linear activation function, even if it is as simple as a bilinear,  
101 function [e.g., Rectified Linear Unit:  $\text{ReLU}(z)=\max(0,z)$ ], plays a critical role that empowers  
102 an FC neural network to capture the complex non-linear patterns in the data.

103



Input layer    Layer 1    Layer 2    Layer 3    Output

(a)



Output vector for the previous layer

Node  $i$  in layer  $l$

Output for node  $i$  in layer  $l$

(b)

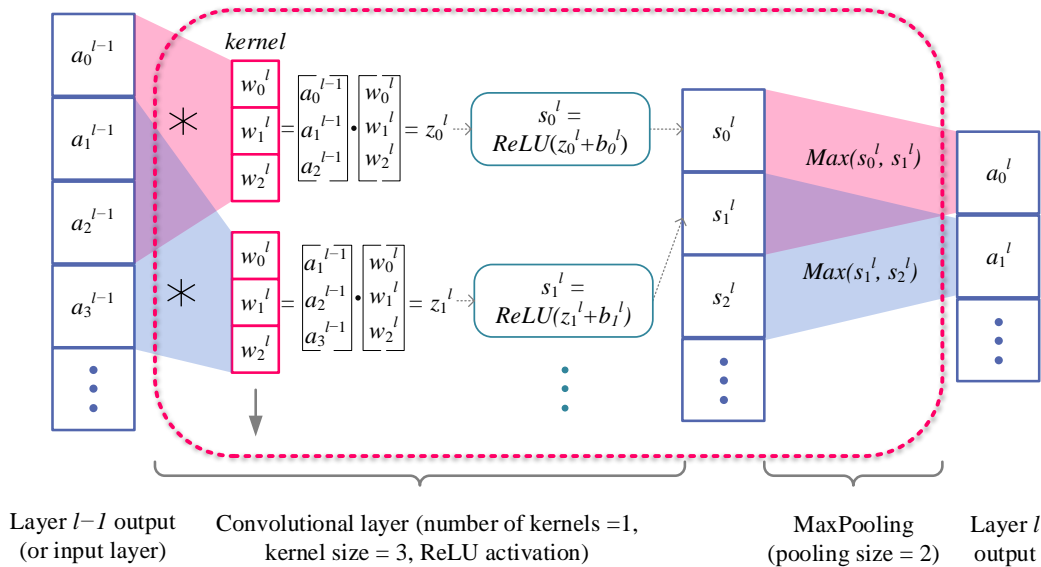
104

105 Figure 1 (a) Architecture of a typical FC neural network.  $a_i^l$  denotes the output of node  $i$  in  
 106 layer  $l$ . Layer 0 is the input layer in the network.; (b) The operation of a node in an FC neural  
 107 network.  $\mathbf{A}^{l-1}$  is the output vector for layer  $l-1$ , which consists of nodes denoted by  $a_0^{l-1}$  to  
 108  $a_m^{l-1}$ .  $\mathbf{w}_i^l$  is a vector of weights for node  $i$  in layer  $l$ .  $b_i^l$  is the bias for node  $i$  in layer  $l$ .  $z_i^l$  is an  
 109 intermediate variable for node  $i$  in layer  $l$ .

110 Convolutional neural network (CNN) is another branch of DL that is often used to  
 111 capture higher-order features from structured data such as images (Patterson and Gibson 2017).  
 112 The application of CNN models for image recognition is one of the primary reasons for the  
 113 thriving of CNN and DL models in the past decade. Convolutional blocks are the fundamental  
 114 elements in a CNN model. A convolutional block often consists of three types of operations:

115 convolution, non-linear activation, and pooling. Figure 2 illustrates the detailed mechanisms of  
 116 these operations using one one-dimensional (1D) convolutional layer with a single kernel as an  
 117 example. In contrast to the two-dimensional (2D) CNNs that are often used for image  
 118 classification, we use a 1D CNN in this study to capture patterns in the CPT data (in the format  
 119 of a 1D vector). When compared with an FC network, a CNN involves significantly fewer  
 120 model parameters that need to be learned considering inputs of the same size, substantially  
 121 reducing the computational cost for model training and inference.

122 Pooling layers are useful for reducing the dimensions of the data, the number of  
 123 parameters to learn, and consequently the computational cost. In this study, the MaxPooling  
 124 function is used, which selects the maximum value within a specified region of data after the  
 125 convolution. Pooling also make models more robust to positional variations in the data.



126

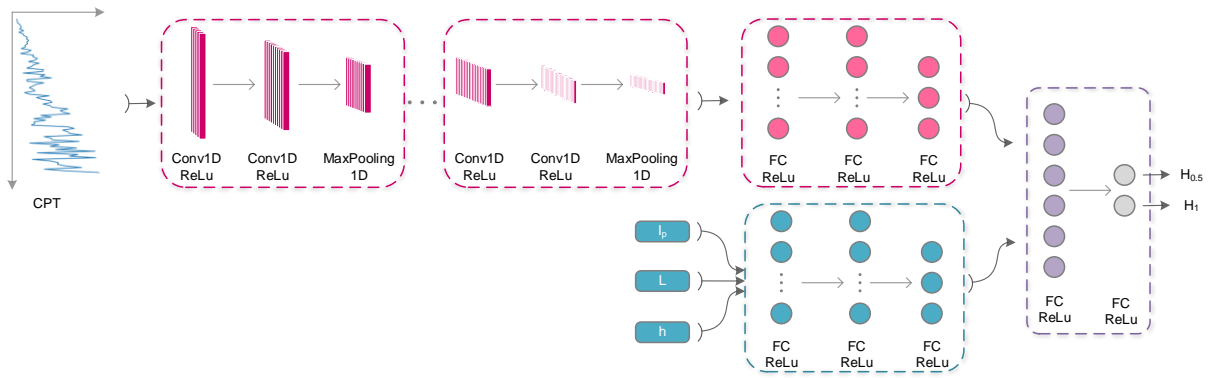
127 Figure 2 Components for a one-dimensional convolutional neural network.  $a_i^{l-1}$  is the output  
 128  $i$  in layer  $l-1$ .  $w_i^l$  represents the  $i^{\text{th}}$  weight in a kernel vector (also known as filter) in layer  $l$ .  
 129 The symbol  $\star$  denotes the convolution operation. The result of convolution operation ( $=z_i^l$ )  
 130 along with a bias term  $b_i^l$  is passed into the non-linear activation function, outputting  $s_i^l$ . Both  
 131  $w_i^l$  and  $b_i^l$  are parameters that need to be learned for layer  $l$ .



132 A key process in the development of a deep learning model is designing the neural  
133 network architecture and selecting the hyperparameters of the model, such as the network's  
134 depth (number of layers), width (number of nodes/kernels), and the type of layers. Deeper and  
135 wider models are more effective in identifying complex patterns in the dataset, but it is more  
136 computationally costly to train the large number of parameters in these more complex models.

137 If the model's performance on the training set continues to improve while its  
138 performance on the validation set starts to deteriorate, it is a sign of overfitting. Training should  
139 be stopped. Complex models are more prone to overfitting the training data, leading to poor  
140 model generalization on new unseen data that is different from the training data. Regularization  
141 techniques (e.g., dropout, L2 regularization and batch normalization) can be used to reduce the  
142 chance of overfitting and improve the model's generalization ability. Simple models, on the  
143 other hand, are easier to train and optimize, but they might not be able to capture the more  
144 complex patterns in a dataset. Often, the development of an ideal model requires repetitive  
145 experimentation guided by monitoring the model errors during training and validating.

146 Figure 3 shows the architecture of the hybrid neural network designed in this study. The hybrid  
147 model consists of two threads of neural network layers. In one thread, convolutional layers  
148 followed by three FC layers are used to capture the patterns (feature extraction: peaks and  
149 valleys that represent strong and weak soil layers) in the CPT cone resistance profile. In the  
150 other thread, FC layers are used to capture the impact of the pile geometry (i.e., area moment  
151 of inertia  $I_p$  and pile length  $L$ ) and loading condition (load eccentricity  $h$ ) on the lateral capacity  
152 of monopiles. Near the end of the model, the two threads are merged into one using FC layers  
153 to capture the impact of the soil-pile interaction on the lateral load response of monopiles. The  
154 final outputs of the model are the lateral pile capacities  $H_{0.5}$  and  $H_1$  corresponding to pile  
155 rotation  $\theta=0.5^\circ$  and  $\theta=1^\circ$ , respectively, at the mudline.



156

157 Figure 3 The architecture of the hybrid neural network model. Convolutional blocks are  
 158 incorporated to extract patterns in the CPT cone resistance profile. Each convolutional block  
 159 contains two one-dimensional convolutional followed by a one-dimensional pooling layer. In  
 160 addition to the CPT data, three geometric attributes of the pile and loading condition are  
 161 introduced to the model with three fully connected layers. In the end, two branches are  
 162 combined to generate the lateral capacities  $H_{0.5}$  and  $H_1$ .

163 **2.2. Data generation and processing**

164 **2.2.1. Data generation**

165 As a data-driven method, a deep learning model often requires a large amount of  
 166 training data to learn the complex relationships between input and output variables (e.g. pile  
 167 geometry, soil profile, loading condition and the lateral pile capacities). Yet, data is limited for  
 168 full-scale lateral load tests on large-diameter monopiles accompanied by full site  
 169 characterization (Byrne et al. 2019; Spill et al. 2017). Alternatively, we can rely on data  
 170 generated from high-quality 3D finite element (FE) analyses. To obtain a sufficient amount of  
 171 data for training the proposed DL model, we used the 3D FE analysis results from Hu et al.  
 172 (2021, 2022). In their study, high-fidelity 3D FE analyses were performed in Abaqus Explicit  
 173 (ABAQUS 2014) to model the response of laterally loaded monopiles in multi-layered sandy  
 174 soil. As shown in Figure 4, only half of the soil-pile domain was modeled in the FE analyses

175 due to the symmetric nature of the boundary value problem. Hexahedral linear elements with  
176 reduced integration (i.e., C3D8R elements) were used in the FE model. To minimize the  
177 boundary effect, the width of the soil domain was set at 20 times the pile diameter, and the  
178 thickness was set at twice the pile length. Given the large pile diameters of monopiles, fully-  
179 coring mode was assumed, and thus both the soil inside and outside the pipe pile was modeled.  
180 The pile-soil interface was modeled following the perfect-contact approach, where the common  
181 nodes of the soil and pile are tied to each other. This was chosen due to the negligible difference  
182 in lateral load response of monopiles modeled by the perfect-contact approach and the contact-  
183 pair approach, as demonstrated by Hu et al. (2021).

184         A two-surface-plasticity sand model developed by Loukidis and Salgado (2009) was  
185 used in the analyses. Developed under a critical-state soil mechanics framework, the  
186 constitutive model closely captures mechanical behavior of sand under various stress paths.  
187 The model was calibrated against elemental test results (e.g., triaxial compression, triaxial  
188 extension, and simple shear) for Ottawa sand and Toyoura sand. With the properly-prepared  
189 mesh (Figure 4) and the realistic constitutive model, the FE analyses are able to accurately  
190 capture the stress-path dependent soil behavior, strain localization in soil, and the soil-pile  
191 interactions. The analyses were performed under fully drained condition using the effective  
192 stress approach given the relatively small loading rate for sandy soil (Han et al. 2017).  
193 Furthermore, the strain localization is controlled by the mesh size: the minimal mesh size is  
194 needs to be comparable to the shear band thickness expected in the sand. This technique has  
195 been used and verified by Loukidis and Salgado (2008) and Han et al. (2017).

196         To validate the 3D FE analyses, Hu et al. (2021) and Hu et al. (2022) compared the  
197 results obtained from their FE analyses with those obtained from the full-scale lateral pile load  
198 tests performed as a part of the Pile Soil Analysis (PISA) project (Byrne et al. 2019; McAdam

199 et al. 2019). The pile load test was performed on a 10.5-m-long, 2-m-diameter open-ended steel  
 200 pipe pile in medium dense to dense marine sand. The predicted and measured load–deflection  
 201 curves at the mudline are in very close agreement.

202 The dataset contains a large number (100000) of data points (also known as samples),  
 203 each consisting of the input values (i.e., area moment of inertia for the pile cross section, pile  
 204 length, CPT  $q_c$  profile, and load eccentricity) and the corresponding outputs (i.e., lateral pile  
 205 capacities  $H_{0.5}$  and  $H_1$  corresponding to pile rotation  $\theta=0.5^\circ$  and  $\theta=1^\circ$  at the mudline). In this  
 206 research, CPT profile is directly used in the model instead of  $D_R$  for two reasons. First, to use  
 207 a  $D_R$ -based model (or other soil property-based models), in-situ test results (such as  $q_c$ ) must  
 208 be converted to  $D_R$ . This conversion may introduce errors originating from factors such as  $K_0$ ,  
 209 unit weight, water table, and friction angle. A CPT-based model can bypass the calculation of  
 210  $D_R$  from  $q_c$  and directly take  $q_c$  profile as the model input. Furthermore, a CPT-based model is  
 211 convenient for the users to apply, where they can directly input the CPT results into the model  
 212 to obtain predictions for the lateral pile capacities without the need to estimate or assume soil  
 213 properties. The CPT cone resistance profile is obtained using the Salgado and Prezzi (2007)  
 214 equation developed based on cavity expansion theory:

$$q_c = 1.64p_A \exp[0.1041\phi_c + (0.0264 - 0.0002\phi_c)D_R] \left(\frac{\sigma'_h}{p_A}\right)^{0.841-0.0047D_R} \quad \text{Eq. 1}$$

215 where  $p_A$  = reference stress = 100kPa,  $\phi_c$  = critical-state friction angle in sand,  $D_R$  = relative  
 216 density in sand ( $D_R=60$  for 60% relative density), and  $\sigma'_h$  = horizontal effective stress. Eq. 1  
 217 has been tested in many prior studies (Han et al. 2017, 2019; Sakleshpur et al. 2021), and it  
 218 provides  $q_c$  values that are consistent to those estimated using the NGI method (Clausen et al.  
 219 2005):

$$q_c = \exp(D_R/0.4)[22(\sigma'_v p_A)^{0.5}] \quad \text{Eq. 2}$$

220 where  $D_R$  is expressed as fractions (e.g.  $D_R=0.6$  for 60% relative density), and  $\sigma'_v$  = vertical  
221 effective stress.

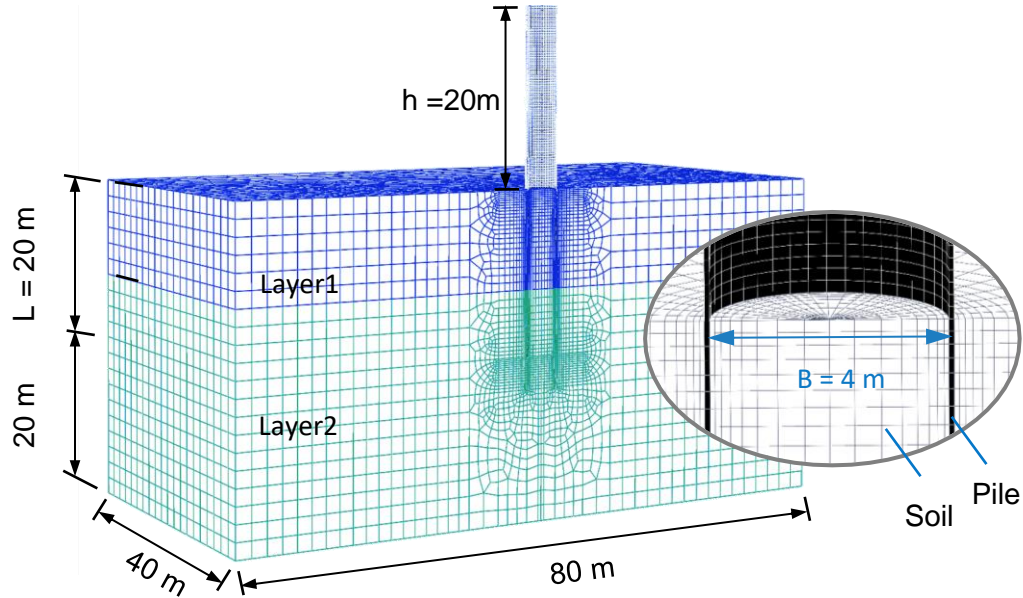


Figure 4 Finite element (FE) analyses of laterally loaded monopiles  
(modified after Hu et al. 2022)

222

223 In order to obtain a robust DL model that is applicable to common design scenarios, the  
224 training samples should cover an extensive range of values for the input variables. Therefore,  
225 we consider broad-ranging values for pile length (6 m to 60 m), pile diameter (2 m to 10 m),  
226 load eccentricity (15 m to 30 m), pile diameter-to-wall-thickness ratio (40 to 100), and the  
227 relative density (35% to 90%) for the multi-layered sandy soils. All raw data used in this study  
228 is published in an open-access data repository (details provided in the data availability section).

229 Since the CPT data (in the format of 1D vectors) vary in size depending on the pile  
230 length, we used Zero Padding (i.e., appending zeros to the end of the original data) to convert  
231 all CPT data into the same size. This is done because CNN accepts data of the same size as the  
232 input. This technique does not affect the predictions as the soil profile in the top layers controls

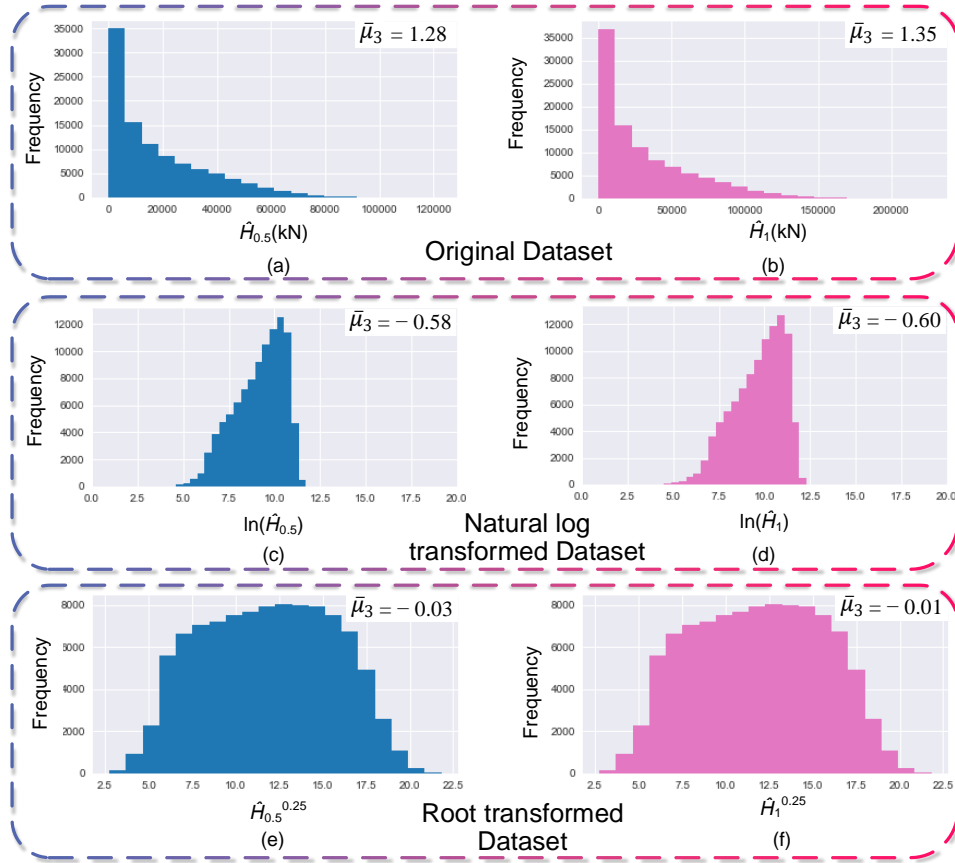
233 the behavior of laterally loaded piles. Alternatively, Recurrent Neural Network (RNN), which  
234 is often used to deal with sequential data, can be used to handle input data of different sizes.

### 235 **2.2.2. Data transformation**

236 When generating the training samples, we maintained a uniform distribution for the  
237 input variables. For example, a pile diameter within the range from 2 m to 10 m is randomly  
238 selected for each sample. However, the uniform distribution for the input variables results in a  
239 highly non-symmetric, non-uniform distribution for the output values (i.e., pile capacities). In  
240 statistics, symmetry of a distribution about its mean can be measured by skewness  $\bar{\mu}_3$  (e.g.,  
241 skewness = 0 represents a completely symmetric distribution):

$$\bar{\mu}_3 = \mathbb{E} \left[ \left( \frac{x - \mu}{\sigma} \right)^3 \right] \quad \text{Eq. 3}$$

242 where  $x$  is the value of a data point in the distribution,  $\mu$  is the mean of the distribution, and  $\sigma$   
243 is the standard deviation of the distribution. As shown in Figure 5a and Figure 5b, the  
244 distribution of the outputs (i.e., pile capacities) for the training dataset is positively skewed (the  
245 distribution is concentrated toward the left side). There is significantly larger amount of data  
246 for piles with smaller lateral capacities, leading to better model performance and higher  
247 prediction accuracies for these piles. Conversely, piles with larger lateral capacities have less  
248 data for model training, leading to greater prediction errors for those piles. To reduce the dataset  
249 skewness and improve overall model performance, we will explore the effectiveness of two  
250 transformation methods (Atkinson et al. 2021):



251

252 Figure 5 Histograms of the outputs and transformed outputs in the generated dataset: (a) The  
 253 distribution of the lateral capacity  $\hat{H}_{0.5}$  corresponding to  $\theta=0.5^\circ$ ; (b) The distribution of the  
 254 lateral capacity  $\hat{H}_1$  corresponding to  $\theta=1^\circ$ ; (c) The distribution of the intermediate output  
 255  $\ln(\hat{H}_{0.5})$  after the natural logarithm transformation. (d) The distribution of the intermediate  
 256 output  $\ln(\hat{H}_1)$  after the natural logarithm transformation. (e) The distribution of the  
 257 intermediate output  $\hat{H}_{0.5}^{0.25}$  after the root transformation. (f) The distribution of the  
 258 intermediate output  $\hat{H}_1^{0.25}$  after the root transformation.

259 Natural log transformation

260 The natural log transformation is one of the most widely used methods to reduce  
 261 skewness of a dataset when it is positively skewed, which is the case for the outputs ( $\hat{H}_{0.5}$  and  
 262  $\hat{H}_1$ ) in our dataset. Thus, we introduce a pair of intermediate outputs  $\hat{Y}_{0.5} = \ln(\hat{H}_{0.5})$  and  $\hat{Y}_1 =$   
 263  $\ln(\hat{H}_1)$  that are used to train the DL model. Note that  $\hat{H}$  and  $\hat{Y}$  refer to the ground-truth values  
 264 whereas  $H$  and  $Y$  refer to the predicted values. As seen in Figure 5c and Figure 5d, the natural  
 265 log transformation reduced the absolute value of skewness ( $|\bar{\mu}_3|$ ) for the original dataset by

266 more than 60% from about 1.3 to 0.6. After DL model training was done, the predicted  
267 intermediate outputs were transformed back to their original form to provide predictions for  
268 pile capacities:  $H_{0.5} = \exp(Y_{0.5})$  and  $H_1 = \exp(Y_1)$ .

### 269 Root transformation

270 Another widely-used transformation method for positively skewed data is root-  
271 transformation. In this study, the fourth root transformation was implemented to convert the  
272 original outputs (pile capacities  $\hat{H}_{0.5}$  and  $\hat{H}_1$ ) into intermediate outputs  $\hat{Y}_{0.5} = (\hat{H}_{0.5})^{0.25}$  and  $\hat{Y}_1$   
273  $= (\hat{H}_1)^{0.25}$  for model training. The root transformation was successful in bringing the skewness  
274 of the original outputs down to almost zero (Figure 5e and Figure 5f). After the DL model was  
275 trained, these intermediate outputs were transferred back to their original form:  $H_{0.5} = (Y_{0.5})^4$   
276 and  $H_1 = (Y_1)^4$ .

### 277 **2.2.3. Input normalization**

278 When training a DL model, the learning algorithm (e.g., Gradient Descent) iteratively  
279 updates the model parameters such that the prediction error is minimized. When the ranges for  
280 the input variables are significantly different (e.g., one input ranges from 1 to 2, whereas  
281 another input ranges from 10 to 10,000), the learning algorithm becomes slow or unstable,  
282 sometimes causing the learning to fail (Bishop 1995). To resolve this issue, input variables are  
283 often scaled (e.g., using normalization or standardization) into the same or similar ranges  
284 before they are used for training. In this paper, each input variable ( $X$ ) is normalized with  
285 respect to its maximum and minimum values ( $X_{\max}$  and  $X_{\min}$ ) using the MinMax normalization  
286 function:



$$X_{scaled} = \frac{X - X_{min}}{X_{max} - X_{min}} \quad \text{Eq. 4}$$

287 After the normalization, all scaled input variables  $X_{scaled}$  fall between 0 and 1.

#### 288 **2.2.4. Training, validation, and test sets**

289 In the development of a DL model, the full dataset is typically split into three separate  
290 subsets (i.e., training, validation, and test sets) that are used for different purposes. The largest  
291 portion of the full dataset is used to train the model parameters (e.g., the weights and biases  
292 shown in Figure 1) in the DL model, hence the name training set. Then, a small portion of the  
293 full dataset (separate from the training set), known as the validation set, is used to evaluate the  
294 model performance to avoid overfitting and underfitting issues. In case of unsatisfactory model  
295 performance, the hyperparameters, such as the learning rate, number of layers, and number of  
296 nodes in each layer, are adjusted, and the model is trained again using the training set. These  
297 two steps are repeated iteratively until satisfactory model performance is obtained for both the  
298 training and validation datasets. Finally, the trained model is assessed against the test dataset  
299 that has never been seen by the model. In this project, the training, validation, and test sets  
300 contain 90%, 5%, and 5% of the full dataset, respectively.

301 The hybrid neural network was implemented using Python 3.9.7 programming  
302 language with Pytorch 1.10.2 as the DL framework. The training was conducted on a computer  
303 with the CPU of Intel Core-i9-10920X, Memory of 128 GB, and GPU of NVidia RTX A5000.  
304 It's worth pointing out that the model's training process was time consuming, taking  
305 approximately 20 hours. However, after the training is finished, generating a prediction from  
306 input values using the trained model takes only a fraction of a second.

## 307 3 RESULTS AND DISCUSSION

### 308 3.1. Results

309 A DL model is trained to minimize errors in predicting the outputs. The model error is  
310 quantified using a cost function, which captures the average error between the ground truth and  
311 prediction for all samples. Proper selection of the cost function is one of the keys to obtaining  
312 a good DL model. Among all commonly-seen cost functions, Mean Squared Error (MSE) is  
313 the most widely used for regression problems:

$$MSE = \frac{1}{n} \sum_{i=1}^n (y_i - \hat{y}_i)^2 \quad \text{Eq. 5}$$

314 where  $n$  is the number of samples,  $y_i$  is the predicted output for the  $i^{\text{th}}$  sample, and  $\hat{y}_i$  is the  
315 corresponding ground truth. Each cost function has its own limitations and strengths. MSE has  
316 a convex topology, which makes the optimization process (i.e., training) to minimize the cost  
317 function more reliable (Aravkin et al. 2014). However, a model trained with MSE equally treats  
318 the absolute error (difference between the predicted and ground-truth outputs) for each sample  
319 regardless of the magnitude of the output. This is problematic when the output variable spans  
320 a wide range of values, as is the case in this study. For example, an error of 100 kN is a 0.1%  
321 relative error for a ground-truth pile capacity of 100,000 kN, whereas the same error (=100 kN)  
322 is a 100% relative error for a pile capacity of 100 kN.

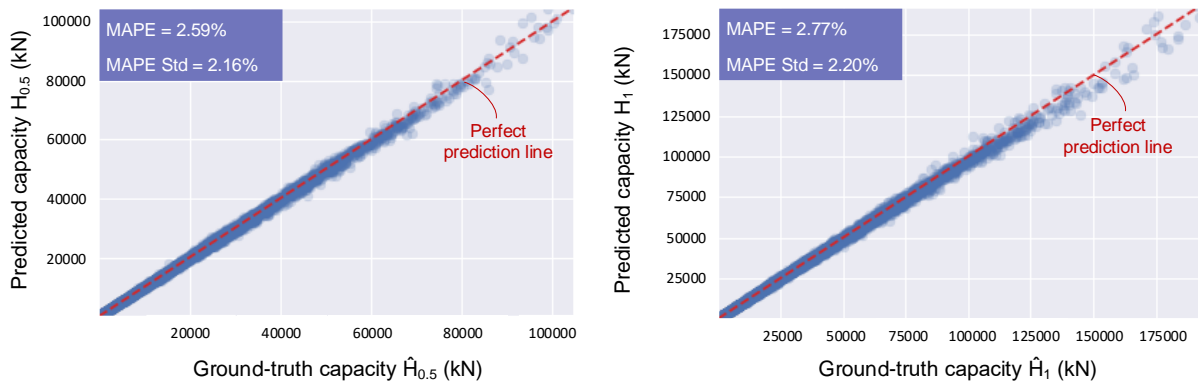
323 To solve the aforementioned issue, we can instead use the Mean Absolute Percentage  
324 Error (MAPE), which calculates the relative error (percentage error) between the predicted  
325 output  $y$  and the ground-truth output  $\hat{y}$ :

$$MAPE = \frac{1}{n} \sum_{i=1}^n \frac{|y_i - \hat{y}_i|}{\hat{y}_i} \times 100 \quad \text{Eq. 6}$$

326 MAPE is often used in practice due to its intuitive interpretation. However, optimizing  
327 MAPE is more computationally challenging than MSE because of its non-convex topology and  
328 non-differentiability (Chen et al. 2017; De Myttenaere et al. 2016).

329 To investigate the effectiveness of different data transformation techniques combined  
330 with different cost functions on the model performance, we used the original dataset, natural  
331 log transformed dataset, and root transformed dataset to train the hybrid neural network model  
332 using either MAPE or MSE as the cost function. The model was trained for 600 epochs (the  
333 number of passes that the algorithm works through the entire training dataset) with a batch size  
334 (the number of training samples the algorithm works through before updating the model  
335 parameters) of 128 and a learning rate (the step size taken to adjust the parameters with respect  
336 to model's error) of 0.001. The learning algorithm is ADAM (Kingma and Ba 2014), which is  
337 an extension of stochastic gradient descent. ADAM is more efficient in training neural  
338 networks with non-convex cost functions.

339 Among the six trained models (i.e., three data transformation techniques combined with  
340 two cost functions), the one trained using natural log transformation and MSE cost function  
341 performs the best, providing consistent predictions with an average relative error  $MAPE = 2.67\%$   
342 for the model outputs. Figure 6 compares the predicted pile capacities  $H_{0.5}$  and  $H_1$  (for pile  
343 rotation  $\theta=0.5^\circ$  and  $\theta=1^\circ$ ) versus the corresponding ground truths  $\hat{H}_{0.5}$  and  $\hat{H}_1$  for this model.  
344 Data points are closely located near the perfect-prediction line, indicating overall good model  
345 performance. We will compare results of the six models in detail in the next section.



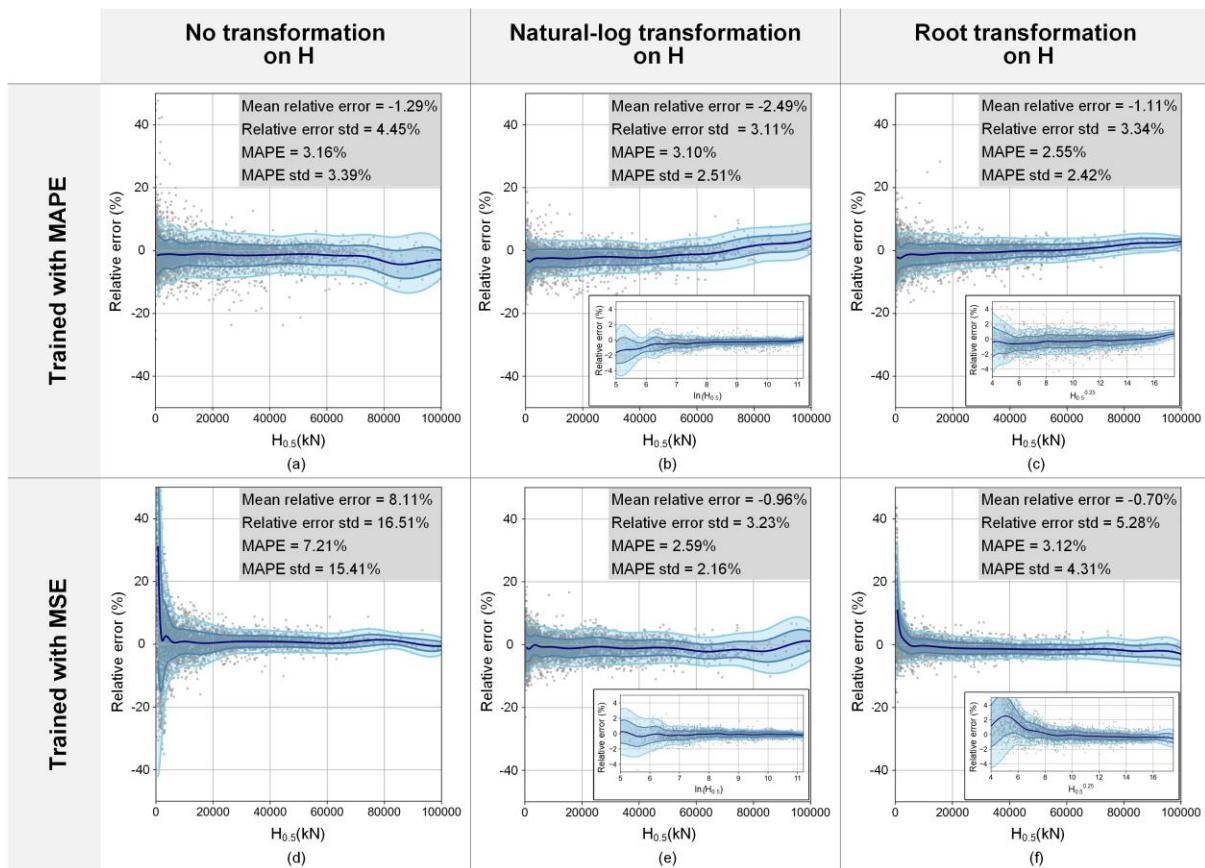
346

347 Figure 6 Performance of the model trained with natural log transformed data and MSE cost  
 348 function: the predicted pile capacities vs. the ground-truth pile capacities.

349 **3.2. Error Analysis**

350 In this section, we analyze errors for each of the six models trained with different data  
 351 transformation techniques and cost functions. Figure 7 shows the relative error  $[(H-\hat{H})/\hat{H}]$  for  
 352 the predicted pile capacity as a function of the ground-truth value for all data points in the test  
 353 set. In addition, we use the concept of Confidence Interval (68% CI and 95% CI) to show the  
 354 probability that the relative error falls within a certain range of values. It is ideal to have the  
 355 mean relative error close to zero and narrow CIs around it, while a wide CI for a certain range  
 356 of pile capacity  $H$  reflects unreliable model predictions for that range of  $H$ . Since the model  
 357 performances in predicting  $H_{0.5}$  and  $H_1$  are similar (Figure 6), we show the error analysis for  
 358  $H_{0.5}$  as an example.

359



360

361 Figure 7 The mean, 68%, and 95% confidence intervals for the models' relative errors in  
 362 predicting pile capacity  $H_{0.5}$ : (a) Relative error for the model trained with MAPE using the  
 363 dataset without transformation; (b) Relative error for the model trained with MAPE using  
 364 natural logarithm transformed data; (c) Relative error for the model trained with MAPE using  
 365 root transformed data; (d) Relative error for the model trained with MSE using the dataset  
 366 without transformation; (e) Relative error for the model trained with MSE using natural  
 367 logarithm transformed data; (f) Relative error for the model trained with MSE using root  
 368 transformed data. Note that the relative error for the intermediate outputs [i.e.,  $\ln(H_{0.5})$  and  
 369  $H_{0.5}^{0.25}$ ] data are presented in the sub-figures.

370 With no data transformation on the pile capacity H, the model trained with MAPE cost  
 371 function results in consistent relative errors for the entire range of pile capacities (Figure 7a),  
 372 whereas training with MSE causes significant relative errors (wider CI) for smaller pile  
 373 capacities (Figure 7d). Since using the MSE cost function minimizes the squared error [ $SE =$   
 374  $(H - \hat{H})^2$ ] between the predictions and ground truths, a model trained with MSE tends to produce

375 predictions for H with consistent SE values across the entire range of H. The consistent SE  
376 values result in absolute percentage errors (APE) that are sensitive to the magnitude of  $\hat{H}$ :

$$MAPE = |H - \hat{H}| / \hat{H} = \sqrt{SE} / \hat{H} \quad \text{Eq. 7}$$

377 Thus, model trained with MSE without any data transformation tends to have larger relative  
378 error (MAPE) for piles with smaller capacity values  $\hat{H}$ , and vice versa (Figure 7d). This is  
379 particularly true when the range of the output values is large, such is the case in this study (the  
380 pile capacity H ranges from about 100 kN to about 100,000 kN).

381 Figure 7b and Figure 7e compare the performance of the two models trained with  
382 natural log transformation using MSE vs MAPE cost functions. After the natural logarithm  
383 transformation, the range for the intermediate output  $\ln(\hat{H})$  shrinks drastically from the range  
384 for the original target output  $\hat{H}$  (Figure 5). The mean decreases from 18633 for  $\hat{H}_{0.5}$  to 9.14 for  
385 the intermediate output  $\ln(\hat{H}_{0.5})$ , and the associated standard deviation (std) decreases from  
386 18621 for  $\hat{H}_{0.5}$  to 1.37 for  $\ln(\hat{H}_{0.5})$ . According to Eq. 7, when the ground-truth output [i.e., the  
387 intermediate output  $\hat{Y} = \ln(\hat{H})$ ] for a model has a small range of values, training the model with  
388 either MSE or MAPE cost function does not make a significant difference in the model  
389 performance for predicting the intermediate output Y (sub figures in Figure 7b and Figure 7e).  
390 This eventually results in similar model performances in predicting the ground-truth  $\hat{H}$   
391 [transformed back from Y to  $H = \exp(Y)$ ], as shown in Figure 7b and Figure 7e.

392 Root transformation also reduces the range for output values (Figure 5). The mean  
393 decreases from 18633 for  $\hat{H}_{0.5}$  to 10.39 for the intermediate output  $\hat{Y} = \hat{H}_{0.5}^{0.25}$ , and the  
394 associated standard deviation (std) decreases from 18621 for  $\hat{H}_{0.5}$  to 3.23 for  $\hat{Y} = \hat{H}_{0.5}^{0.25}$ . Yet,  
395 root transformation does not reduce the output range as much as natural logarithm  
396 transformation does (Figure 5). Consequently, we see greater relative errors (i.e., wider CIs)

397 for smaller intermediate outputs ( $\hat{H}^{0.25}$ ) for the model trained with MSE cost function (sub  
398 figure in Figure 7f), leading to the large relative errors for smaller pile capacities  $\hat{H}$  (Figure 7f).

399 Among the six models considered in this study, the model trained with MSE using  
400 natural logarithm transformed data is the most reliable one with MAPE = 2.59% and MAPE  
401 std = 2.16%. The model trained with MAPE using root transformation has a slightly smaller  
402 MAPE value (=2.55%) yet a greater std value (MAPE std = 2.42%).

### 403 3.3. Which cost function and data transformation methods to choose?

404 We often deal with geotechnical data that has a wide range of values with large data  
405 skewness due to the inherent variability and nonlinearity in the underlying geotechnical  
406 problems (e.g., pile capacities, footing settlement, and slope deformation). When developing a  
407 deep learning model to solve these problems, it is crucial to choose an appropriate combination  
408 of data transformation method and cost function to tackle the extensive range and skewed  
409 nature of the data. In this section, we derive theoretical errors and relative errors expected from  
410 using different data transformation techniques and cost functions.

411 Table 1 summarizes how an error  $E$  (or relative error  $E_r$ ) associated with the  
412 intermediate output  $Y$  (at the end of training) is transformed to be the error (or relative error)  
413 for the target variable  $H$ . For example, a relative error  $E_r$  for the intermediate output  $Y=\ln(H)$   
414 (i.e., natural log transformation) results in a relative error of  $\hat{H}^{E_r}-1$  for the target output  $H$ . This  
415 means when the model is trained with MAPE cost function, which ideally tends to produce  
416 consistent relative error  $E_r$  for the whole range of intermediate output  $Y$ , the relative error  
417 ( $=\hat{H}^{E_r}-1$ ) for the target output  $H$  becomes dependent on the value of  $\hat{H}$ : The relative error for  $\hat{H}$   
418 tends to increase with increasing  $\hat{H}$ . As shown in Table 1, among the four combinations of data  
419 transformation methods and cost functions, training the model with natural log transformation

420 in conjunction with MSE cost function or training with root transformation in conjunction with  
421 MAPE cost function will result in consistent relative errors for the target output H that is  
422 independent of the value of H (or  $\hat{H}$ ).

423         Ideally, a model trained with the MSE cost function tends to produce predictions with  
424 zero-mean randomly distributed errors (i.e., mean of errors=0). Similarly, a model trained with  
425 MAPE cost functions tends to produce predictions with zero-mean randomly distributed  
426 relative errors (i.e., mean of relative errors=0). In Figure 8, we further demonstrate how errors  
427 or relative errors for the intermediate output Y propagate into the relative error for the target  
428 output H. We assume a zero-mean evenly-distributed error or relative error for the intermediate  
429 output Y depending on the training cost functions. The second row of sub-figures shows the  
430 corresponding relative errors for the target variable H after the intermediate variable Y is  
431 transformed to H. As suggested by Table 1, training with two specific combinations of cost  
432 function and data transformation (MSE with log transformation and MAPE with root  
433 transformation) leads to consistent relative errors for the target output H. This is reflected in  
434 Figure 8 (bottom-left and bottom right sub-figures) as randomly distributed zero-mean relative  
435 errors that are independent of the value of H. In contrast, Training the model with log  
436 transformation and MAPE loss function causes the relative error for the target output H to  
437 increase with increasing value of H. Training the model with root transformation and MSE loss  
438 function results in decreasing relative errors for the target output H as H increases. These two  
439 combinations should be avoided in data treatment and model training to prevent inconsistent  
440 relative errors for predictions depending on the output value.

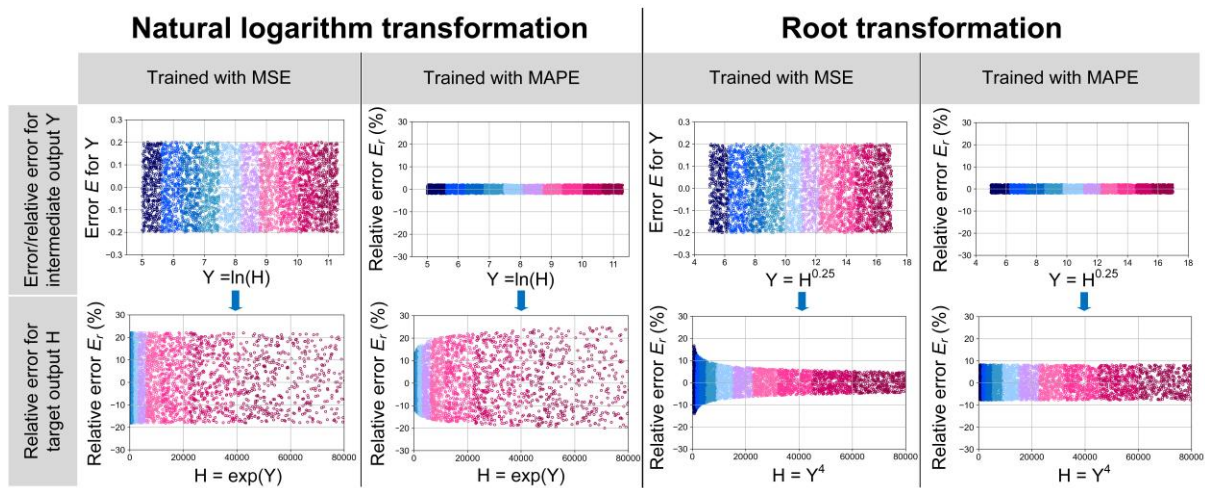


441 Table 1 Error analysis for different data transformation methods (for model outputs) trained  
 442 with different cost functions

Type of transformation	Natural log	Natural log	Root	Root
Intermediate output $\hat{Y}$ after transformation	$\hat{Y} = \ln(\hat{H})$	$\hat{Y} = \ln(\hat{H})$	$\hat{Y} = \hat{H}^\alpha$	$\hat{Y} = \hat{H}^\alpha$
Cost function	MSE	MAPE	MSE	MAPE
Error to be minimized*	$E^2 = (Y - \hat{Y})^2$	$ E_r  =  Y - \hat{Y} /\hat{Y}$	$E^2 = (Y - \hat{Y})^2$	$ E_r  =  Y - \hat{Y} /\hat{Y}$
Predicted intermediate output $Y$	$Y = \hat{Y} + E$	$Y = \hat{Y}(1 + E_r)$	$Y = \hat{Y} + E$	$Y = \hat{Y}(1 + E_r)$
Transformation back to target output $H$	$H = e^Y = e^{\hat{Y} + E}$	$H = e^Y = e^{\hat{Y}(1 + E_r)}$	$H = Y^{(1/\alpha)} = (\hat{Y} + E)^{(1/\alpha)}$	$H = Y^{(1/\alpha)} = [\hat{Y}(1 + E_r)]^{(1/\alpha)}$
Error for target output $H (= H - \hat{H})$	$e^{\hat{Y} + E} - e^{\hat{Y}}$	$e^{\hat{Y}(1 + E_r)} - e^{\hat{Y}}$	$(\hat{Y} + E)^{(1/\alpha)} - (\hat{Y})^{(1/\alpha)}$	$[\hat{Y}(1 + E_r)]^{(1/\alpha)} - \hat{Y}^{(1/\alpha)}$
Relative error for target output $H [= (H - \hat{H})/\hat{H}]$	$e^E - 1^{**}$	$\hat{H}^{E_r} - 1$	$(1 + E/\hat{H}^\alpha)^{(1/\alpha)} - 1$	$(1 + E_r)^{(1/\alpha)} - 1^{**}$

443 \*E is the error for the predicted intermediate output Y:  $E = Y - \hat{Y}$ ;  $E_r$  is the relative error for the predicted intermediate  
 444 output Y:  $E_r = (Y - \hat{Y})/\hat{Y}$ .

445 \*\*These two combinations of cost function and data transformation result in consistent relative errors for the target output  
 446 H that is independent of the value of H (or  $\hat{H}$ ).  
 447

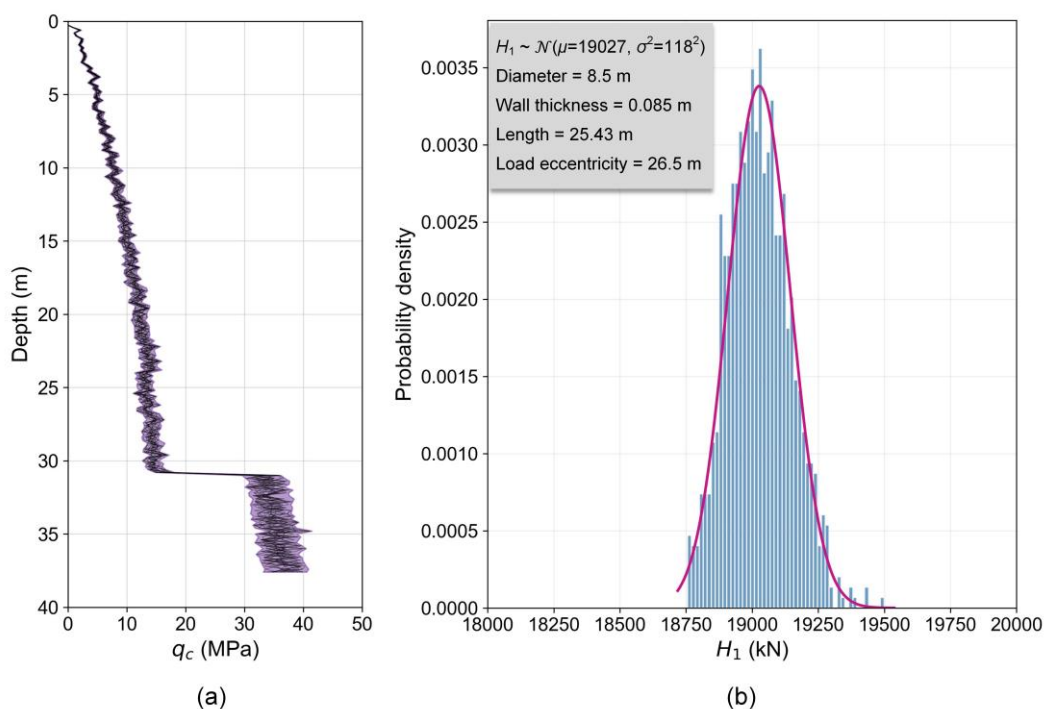


448  
 449 Figure 8- The propagation of error/relative error for the intermediate output Y to the relative  
 450 error for the target output H. Random error E ranging from  $-0.2$  to  $0.2$  is assumed for the  
 451 intermediate output Y when training with the MSE loss function. Random relative error  $E_r$   
 452 ranging from  $-2\%$  to  $2\%$  is assumed for the intermediate output Y when training with the  
 453 MAPE loss function. Data points marked with the same color are associated with the same  
 454 samples before and after data transformation.

#### 455 3.4. Sensitivity analysis for the $q_c$ profile

456 To evaluate the susceptibility of the proposed ANN model to noise in the CPT data, a sensitivity  
457 analysis was done for a specific case characterized by a pile diameter of 8.5 m, a length of  
458 25.43 m, and a load eccentricity of 26.5 m. The influence of the CPT data noise on the model  
459 performance was assessed by creating 1000 variations of the  $q_c$  profile. This was achieved by  
460 introducing random noise ranging from -10% to +10% into the baseline CPT data (Figure 9a).  
461 The lateral capacities  $H_l$  predicted based on these 1000  $q_c$  profiles follows a normal distribution  
462 (Figure 9b) with a remarkably low standard deviation (=0.6% of the mean value). This means  
463 that 68% of the predictions have relative errors less than 0.6%. This example shows the  
464 robustness of the proposed ANN model to the noise and uncertainties in the CPT data. The  
465 robustness of the ANN model is due to both the wide range of diverse data used for model  
466 training and the data augmentation technique used for data preparation (by adding noise to the  
467  $q_c$  profiles in training data).

468



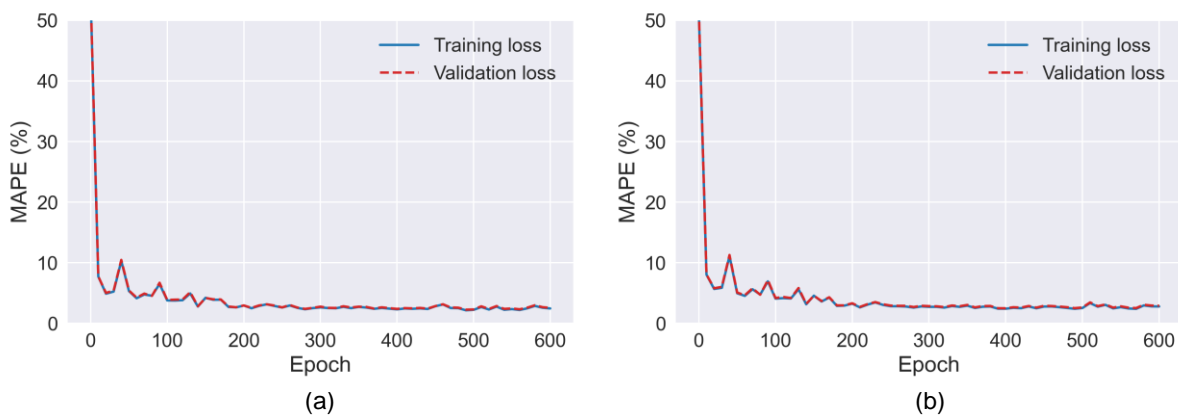
469

470 Figure 9- Sensitivity of the predicted capacity  $H_1$  to the noise in CPT data (a) CPT with  
 471 random relative noise ranging from -10% to +10%. (b) distribution of the pile lateral  
 472 capacities predicted based on the noisy CPT data

473 **3.5. Training histories**

474 When tuning and evaluating a DL model, two model behaviors should be avoided:  
 475 underfitting and overfitting. Underfitting means that the model cannot capture patterns in the  
 476 dataset or identify the relationships between the inputs and outputs; this is reflected in large  
 477 prediction errors for the training set. Overfitting, on the other hand, refers to the case when a  
 478 model can produce good predictions for the training set, but it does not generalize well to the  
 479 validation set, which is unseen by the model during training (Goodfellow et al. 2016; Patterson  
 480 and Gibson 2017). Underfitting occurs when the DL model is too simple (i.e., with a small  
 481 number of layers and nodes) or is not sufficiently trained (too few epochs), while too  
 482 sophisticated model or exceedingly training a model may lead to overfitting.

483 Figure 10 shows the error histories for the model during the training. The MAPE error  
 484 is calculated at the end of each epoch for both the training and validation datasets. As training  
 485 continues, the model parameters keep being updated (by the ADAM training algorithm), and  
 486 the prediction error continues to decrease. As shown in Figure 10, the errors for the training set  
 487 and the validation set decrease following the same trend, suggesting that the model generalizes  
 488 well to the validation set. Hypothetically, if the error for the validation set were significantly  
 489 greater than that for the training set from the beginning of training, the model could be  
 490 overfitted due to too complex model. If the error histories for the two sets first followed the  
 491 same trend until they diverged at some point, that would suggest overfitting due to the model  
 492 being overtrained beyond the divergence point.



493  
 494 Figure 10 The loss history of learning and validation for the model trained with MSE using  
 495 natural log transformation. (a) The loss history for  $H_{0.5}$  (b) The loss history for  $H_1$ .

### 496 3.6. Design example

497 In order to demonstrate the performance of the developed Hybrid neural network model,  
 498 we present a design example from Hu et al. (2022). A pipe pile with a diameter of 5 m, wall  
 499 thickness of 5 cm, and length of 35 m is laterally loaded in multi-layered sandy soil (Figure  
 500 11a). The lateral load is applied at a height of 15 m from the ground surface (load eccentricity

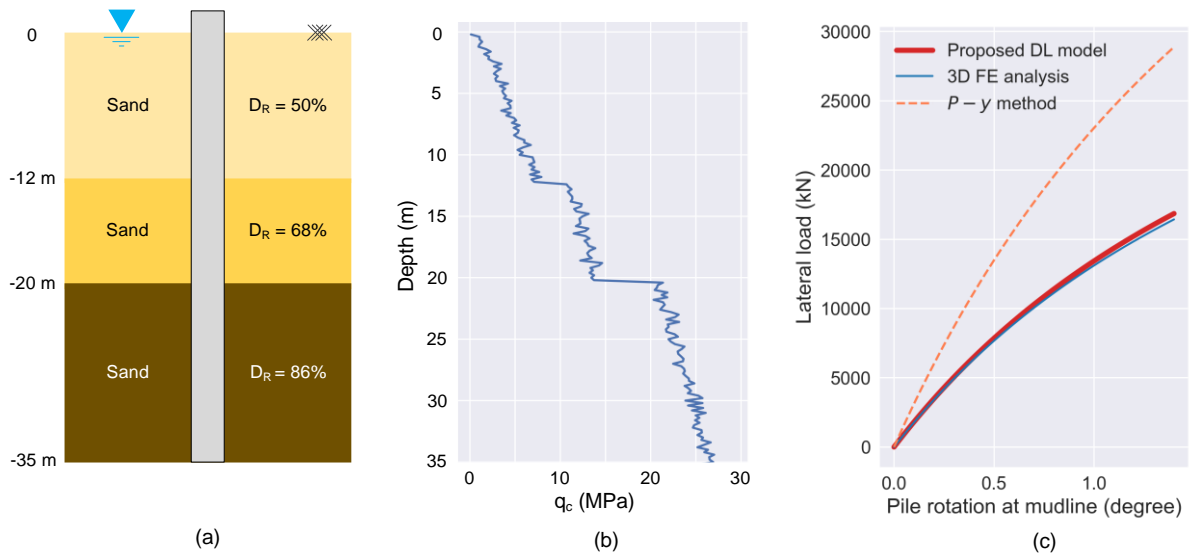
501 h = 15m). The soil is fully saturated with the water table located at the ground surface. Figure  
502 11(b) shows the CPT cone resistance  $q_c$  profile as a function of depth. The pile geometries,  
503 load eccentricity and the CPT  $q_c$  profile were fed into the hybrid neural network model,  
504 producing predictions for the pile lateral capacities  $H_{0.5} = 7858$  kN and  $H_1 = 13442$  kN  
505 corresponding to  $\theta=0.5^\circ$  and  $\theta=1^\circ$ . These two values of pile rotation were chosen because 1)  
506 they represent the serviceability limit states of the pile, and 2) they can be used to develop the  
507 entire load-rotation (H- $\theta$ ) response for this monopile using (Eq. 8) proposed by Hu et al.  
508 (2022b):

$$H = \frac{\theta}{k + \eta\theta}$$

$$\begin{cases} \eta = 2/H_1 - 1/H_{0.5} \\ k = 1/H_{0.5} - 1/H_1 \end{cases} \quad (\text{Eq. 8})$$

509 For comparison purposes, the p-y analysis was performed for this pile using the web-  
510 based application [Lateral Analysis of Piles (LAP)] (Doherty 2017). A three-layer soil profile  
511 (Figure 11a) was considered in the p-y analysis using the API sand p-y curves. The 3D FE  
512 analysis was performed following the simulation setup detailed in Hu et al. (2022). As shown  
513 in Figure 11b, the proposed DL model provides accurate predictions for the lateral load  
514 response of the monopile. The p-y analysis, which was originally developed for long and  
515 slender piles, significantly overestimates the lateral capacities of the pile (Figure 11c).

516



517

518 Figure 11 (a) Soil profile and the corresponding relative densities and thicknesses; (b) The  
519 CPT cone resistance profile; (c) The load rotation response curves obtained from the 3D FE  
520 model, DL model, and the p-y analysis. The p-y analysis overestimates the lateral pile  
521 capacity by 75%; the DL model could predict the capacity well with a relative error of 2.45%.

#### 522 4 PILE DESIGN OPTIMIZATION

523 Given its ability to deliver rapid and precise predictions, the proposed ANN model can  
524 function as a surrogate model, approximating complex FE models. This allows for the  
525 execution of computation-heavy procedures like design optimization or system modeling that  
526 necessitate the simulation of numerous design instances. Surrogate models substantially cut  
527 down the computational cost of optimization, paving the way for more rapid design iterations  
528 and aiding in pinpointing the most effective solutions. To demonstrate a practical application  
529 of the trained surrogate model, we conduct optimization for a design example aiming to  
530 minimize the material cost for the monopile whiling satisfying a set of constraints, including  
531 specified ranges for slenderness ratio, wall thickness ratio, and the pile diameter as well as  
532 meeting the required lateral capacity. The optimization problem is formulated as:

533  $Min. \quad \rho\pi Bt_wL$

534 *Subject to:*

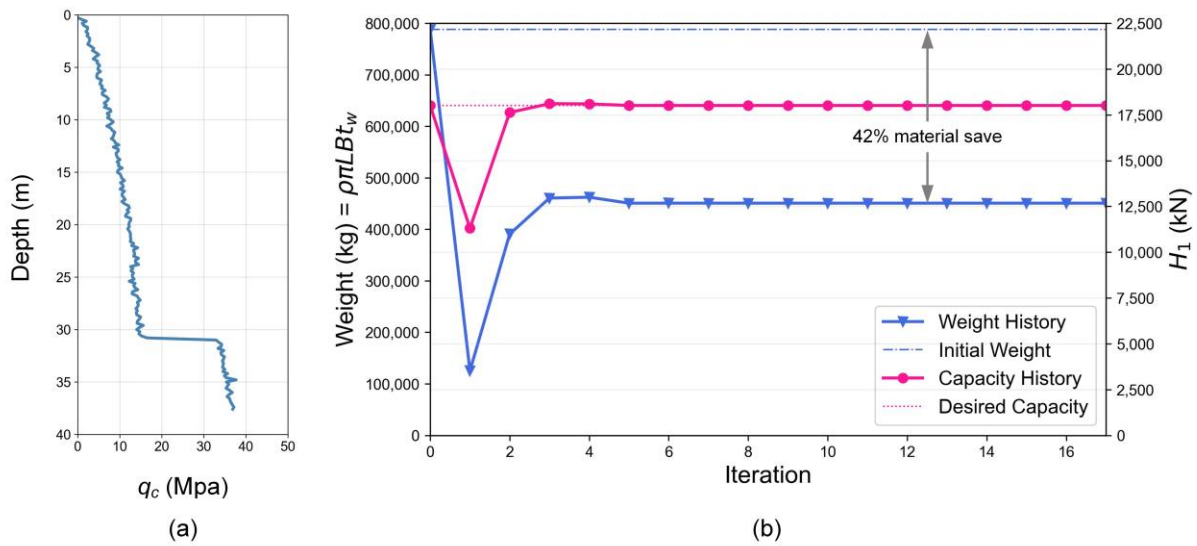
535 (1)  $H_1 \geq \hat{H}_1$

536 (2)  $3 \leq L/B \leq 15$

537 (3)  $40 \leq B/t_w \leq 100$

538 (4)  $2 \leq B \leq 10$

539 where  $B$ ,  $t_w$ , and  $L$  are the pile diameter, wall thickness, and length, respectively.  $H_1$  is the  
540 lateral capacity of the optimized solution, and  $\hat{H}_1$  is the desired capacity. One specific design  
541 example was selected for optimization. The initial pile dimensions are  $B = 6.87$  m,  $t_w = 0.15$  m,  
542  $L = 31$  m, load eccentricity  $h = 26.5$  m, and the corresponding lateral capacity  $\hat{H}_1 = 18007$  kN.  
543 The initial weight of the pile is 787,824 kg. The Sequential Quadratic Programming (SQP)  
544 algorithm was used to optimize the pile design. The SQP algorithm is an iterative optimization  
545 used to solve nonlinear constrained optimization problems. In each iteration, it constructs a  
546 quadratic approximation of the objective function and a linear approximation of the constraints  
547 to form a Quadratic Programming subproblem. The solution to this subproblem then provides  
548 a search direction for an iterative line search procedure, and this process repeats until the  
549 convergence criteria are met or the maximum number of iterations is reached. The SQP  
550 algorithm takes about 10 minutes to output the optimized solution:  $B = 8.5$  m,  $t_w = 0.085$  m,  
551 and  $L = 25.43$  m. This optimized pile design provides the same lateral capacity (18007 kN) as  
552 the original design, but the weight of the optimized pile is 450,676 kg, which is 42% less than  
553 that for the original design. Figure 12 shows the history of the pile weight and the  
554 corresponding pile capacity during the optimization process.



555

556 Figure 12- (a) CPT  $q_c$  profile considered for the pile design optimization example. (b)  
 557 Solution history for the pile design optimization with the objective to reduce the material cost  
 558 for the monopile while providing the required lateral capacity.

559 **5 CONCLUSIONS AND DISCUSSIONS**

560 A hybrid neural network model was developed to provide fast and accurate predictions  
 561 of the lateral capacities for large-diameter monopiles. The neural network contains a series of  
 562 convolutional layers that captures the soil behavior (via CPT cone resistance data) and fully-  
 563 connected layers that accounts for the impact of pile geometry, load eccentricity and the pile-  
 564 soil interactions on the lateral pile load response. To train the model, synthetic data were  
 565 generated based on validated 3D finite element analyses covering a wide range of design  
 566 scenarios. The developed neural network model is able to provide accurate capacity predictions  
 567 (mean average error = 2.68%). The developed ANN model was then integrated into Sequential  
 568 Quadratic Programming (SQP) to optimize pile design, minimizing material cost (by 42%)  
 569 while satisfying the capacity requirement.



570 Highly skewed distribution of the output variables in the training dataset adversely  
571 affects the performance of deep learning models. The natural logarithm transformation and root  
572 transformation techniques can effectively reduce the skewness of the output distribution. These  
573 data transformation techniques need to be used in pairs with specific training cost functions to  
574 achieve the best model performance: The natural logarithm transformation should be used with  
575 the MSE cost function, whereas the root transformation should be used with the MAPE cost  
576 function to provide predictions with consistent relative percentage errors that are independent  
577 of the model output values. This is particularly useful when the output spans a large range of  
578 values.

579 The proposed neural network model has many advantages when compared with high-  
580 fidelity 3D FE model: 1) The proposed model can generate predictions with high accuracy at a  
581 much faster rate compared to a 3D FE model. While a 3D FE analysis may take 2-7 days  
582 depending on the model size (larger piles taking longer runtime due to more elements), the  
583 proposed model can generate predictions in just a fraction of a second. The proposed model is  
584 an excellent surrogate for the 3D FE model, enabling large-scale system-level modeling,  
585 optimization, and resilience analysis; 2) The proposed method is data-driven, and it eliminates  
586 the need for users to possess specialized knowledge, such as meshing and constitutive model,  
587 which are crucial for performing high-quality FE analyses; and 3) Trained with a large dataset  
588 that covers broad-ranging values for design inputs, the developed model is versatile and  
589 adaptable. It can serve as the base model that can be easily adapted for specific design scenarios  
590 (e.g., a special site condition) with only a small amount of data using the transfer learning  
591 technique.

592 The model can be further strengthened in terms of robustness and reliability by training  
593 with more diversified soil types (e.g., over-consolidated soils) and pile types (e.g., concrete

594 piles). This hybrid neural network framework can also be easily extended to solve other  
595 geotechnical problems (e.g., axially loaded piles and shallow foundations).

## 596 **6 DATA AVAILABILITY**

597 The raw dataset used to train the proposed hybrid neural network is published at the  
598 open-access Zenodo data repository (<https://doi.org/10.5281/zenodo.7675229>).

599

600 **NOTATION**

601	$L$	pile length
602	$B$	outer diameter of pile
603	$t_w$	wall thickness of pile
604	$I_p$	area moment of inertia of pile
605	$h$	load eccentricity
606	$D_R$	relative density of sand
607	$\theta$	pile rotation at the mudline
608	$\hat{H}$	ground-truth pile lateral capacity
609	$H$	estimated pile lateral capacity
610	$\hat{H}_{0.5}$	ground-truth pile lateral capacity corresponding to a pile rotation $\theta = 0.5^\circ$
611		at mudline
612	$H_{0.5}$	estimated pile lateral capacity corresponding to a pile rotation $\theta = 0.5^\circ$ at
613		mudline
614	$\hat{H}_1$	ground-truth pile lateral capacity corresponding to a pile rotation $\theta = 1^\circ$ at
615		mudline
616	$H_1$	estimated pile lateral capacity corresponding to a pile rotation $\theta = 1^\circ$ at
617		mudline
618	$\bar{\mu}_3$	skewness of the distribution
619		

620 **7 REFERENCES**

621 ABAQUS. 2014. “ABAQUS 6.14-4.” Abaqus Analysis User’s Manual (RI, USA:  
622 SIMULIA Inc).

623 Adeel, M. B., M. A. Jan, M. Aaqib, and D. Park. 2021. “Development of Simulation  
624 Based p-Multipliers for Laterally Loaded Pile Groups in Granular Soil Using 3D Nonlinear  
625 Finite Element Model.” *Appl. Sci.*, 11 (1): 26. Multidisciplinary Digital Publishing Institute.  
626 <https://doi.org/10.3390/app11010026>.

627 Ahmadi, M. M., and S. Ahmari. 2009. “Finite-element modelling of laterally loaded  
628 piles in clay.” *Proc. Inst. Civ. Eng. - Geotech. Eng.*, 162 (3): 151–163. ICE Publishing.  
629 <https://doi.org/10.1680/geng.2009.162.3.151>.

630 Aravkin, A., J. V Burke, A. Chiuso, and G. Pillonetto. 2014. “Convex vs non-convex  
631 estimators for regression and sparse estimation: the mean squared error properties of ARD and  
632 GLasso.” *J. Mach. Learn. Res.*, 15 (1): 217–252. JMLR. org.

633 Atkinson, A. C., M. Riani, and A. Corbellini. 2021. “The Box–Cox Transformation:  
634 Review and Extensions.” *Stat. Sci.*, 36 (2): 239–255. Institute of Mathematical Statistics.

635 Birba, D. E. 2020. “A Comparative study of data splitting algorithms for machine  
636 learning model selection.”

637 Brown, D. A., and C.-F. Shie. 1990. “Three dimensional finite element model of  
638 laterally loaded piles.” *Comput. Geotech.*, 10 (1): 59–79. [https://doi.org/10.1016/0266-  
639 352X\(90\)90008-J](https://doi.org/10.1016/0266-352X(90)90008-J).

640 Bishop, C. M. 1995. *Neural networks for pattern recognition*. Oxford university press.

641 Byrne, B. W., H. J. Burd, L. Zdravković, R. A. McAdam, D. M. G. Taborda, G. T.  
642 Houlsby, R. J. Jardine, C. M. Martin, D. M. Potts, and K. G. Gavin. 2019. “PISA: new design

643 methods for offshore wind turbine monopiles.” *Rev. Française Géotechnique*, (158): 3. EDP  
644 Sciences.

645 Byrne, B. W., Houlsby, G. T., Burd, H. J., Gavin, K. G., Igoe, D. J., Jardine, R. J., ... &  
646 Zdravković, L. (2020). PISA design model for monopiles for offshore wind turbines:  
647 application to a stiff glacial clay till. *Géotechnique*, 70(11), 1030-1047.

648 Chan, C. L., and B. K. Low. 2012. “Probabilistic analysis of laterally loaded piles using  
649 response surface and neural network approaches.” *Comput. Geotech.*, 43: 101–110. Elsevier.

650 Chen, C., J. Twycross, and J. M. Garibaldi. 2017. “A new accuracy measure based on  
651 bounded relative error for time series forecasting.” *PLoS One*, 12 (3): e0174202.

652 Chatterjee, K., D. Choudhury, and H. G. Poulos. 2015. “Seismic analysis of laterally  
653 loaded pile under influence of vertical loading using finite element method.” *Comput. Geotech.*,  
654 67: 172–186. <https://doi.org/10.1016/j.compgeo.2015.03.004>.

655 Chen, L., and H. G. Poulos. 1993. “Analysis of pile-soil interaction under lateral  
656 loading using infinite and finite elements.” *Comput. Geotech.*, 15 (4): 189–220.  
657 [https://doi.org/10.1016/0266-352X\(93\)90001-N](https://doi.org/10.1016/0266-352X(93)90001-N).

658 Cheng, X., A. Diambra, E. Ibraim, H. Liu, and F. Pisanò. 2021. “3D FE-informed  
659 laboratory soil testing for the design of offshore wind turbine monopiles.” *J. Mar. Sci. Eng.*, 9  
660 (1): 101. MDPI.

661 De Myttenaere, A., B. Golden, B. Le Grand, and F. Rossi. 2016. “Mean absolute  
662 percentage error for regression models.” *Neurocomputing*, 192: 38–48. Elsevier.

663 Doherty, P., and K. Gavin. 2012. “Laterally loaded monopile design for offshore wind  
664 farms.” *Proc. Inst. Civ. Eng. Energy*, 165 (1): 7–17. ICE Publishing.

665 Doherty, J. P. (2017, June). A web-based application for the lateral analysis of pile  
666 (LAP) foundations. In International Conference on Offshore Mechanics and Arctic  
667 Engineering (Vol. 57779, p. V009T10A012). American Society of Mechanical Engineers.

668 Farahani, A., M. Samadzad, and R. Rafiee-Dehkharghani. 2022. “Vibration mitigation  
669 of pile groups by coupling a wave-based vibration analysis and genetic algorithm.” Taylor &  
670 Francis.

671 Goodfellow, I., Y. Bengio, and A. Courville. 2016. Deep learning. MIT press.

672 Han, F., M. Prezzi, and R. Salgado. 2017. “Energy-based solutions for nondisplacement  
673 piles subjected to lateral loads.” *Int. J. Geomech.*, 17 (11): 04017104.

674 Han, F., R. Salgado, and M. Prezzi. 2015. “Nonlinear analyses of laterally loaded piles  
675 – A semi-analytical approach.” *Comput. Geotech.*, 70: 116–129. Elsevier.

676 Han, F., R. Salgado, M. Prezzi, and J. Lim. 2017. “Shaft and base resistance of non-  
677 displacement piles in sand.” *Computers and Geotechnics*, 83: 184–197.

678 Han, F., E. Ganju, R. Salgado, and M. Prezzi. 2019. “Comparison of the load response  
679 of closed-ended and open-ended pipe piles driven in gravelly sand.” *Acta Geotechnica*, 14  
680 (6): 1785–1803. <https://doi.org/10.1007/s11440-019-00863-1>.

681 Hu, Q., F. Han, M. Prezzi, R. Salgado, and M. Zhao. 2021. “Lateral load response of  
682 large-diameter monopiles in sand.” *Géotechnique*, 1–16.

683 Hu, Q., F. Han, M. Prezzi, R. Salgado, and M. Zhao. 2022. “Finite-Element Analysis  
684 of the Lateral Load Response of Monopiles in Layered Sand.” *J. Geotech. Geoenvironmental*  
685 *Eng.*, 148 (4): 04022001. American Society of Civil Engineers.

686 Huang, Y., Z. He, A. Yashima, Z. Chen, and C. Li. 2022. “Multi-objective optimization  
687 design of pile-anchor structures for slopes based on reliability theory considering the spatial  
688 variability of soil properties.” *Comput. Geotech.*, 147: 104751. Elsevier.

689           Kardani, N., A. Zhou, M. Nazem, and S. L. Shen. 2020. “Estimation of Bearing  
690 Capacity of Piles in Cohesionless Soil Using Optimised Machine Learning Approaches.”  
691 Geotech. Geol. Eng., 38 (2): 2271–2291. Springer.

692           Kingma, D. P., and J. Ba. 2014. “Adam: A method for stochastic optimization.” arXiv  
693 Prepr. arXiv1412.6980.

694           Kementzetzidis, E., W. G. Versteijlen, A. Nernheim, and F. Pisano. 2018. “3D FE  
695 dynamic modelling of offshore wind turbines in sand: natural frequency evolution in the pre–  
696 to after-storm transition.” Numer. Methods Geotech. Eng. IX, 2: 1477–1484. CRC Press.

697           Kordjazi, A., F. P. Nejad, and M. B. Jaksa. 2014. “Prediction of ultimate axial load-  
698 carrying capacity of piles using a support vector machine based on CPT data.” Comput.  
699 Geotech., 55: 91–102. Elsevier.

700           Lai, Z., Q. Chen, and L. Huang. 2022. “Machine-learning-enabled discrete element  
701 method: Contact detection and resolution of irregular-shaped particles.” Int. J. Numer. Anal.  
702 Methods Geomech., 46 (1)

703           Loukidis, D., and R. Salgado. 2009. “Modeling sand response using two-surface  
704 plasticity.” Comput. Geotech., 36 (1–2): 166–186.

705           Makasis, N., G. A. Narsilio, and A. Bidarmaghz. 2018. “A machine learning approach  
706 to energy pile design.” Comput. Geotech., 97: 189–203. Elsevier.

707           McAdam, R. A., B. W. Byrne, G. T. Houlsby, W. J. A. P. Beuckelaers, H. J. Burd, K.  
708 G. Gavin, D. J. P. Igoe, R. J. Jardine, C. M. Martin, A. Muir Wood, D. M. Potts, J. Skov  
709 Gretlund, D. M. G. Taborda, and L. Zdravković. 2019. “Monotonic laterally loaded pile testing  
710 in a dense marine sand at Dunkirk.” Géotechnique, (July): 1–13.

711           McAdam, R. A. (2020). Finite-element modelling of laterally loaded piles in a dense  
712 marine sand at Dunkirk. Géotechnique, 70(11), 1014-1029.

713           McCulloch, W. S., and W. Pitts. 1943. "A logical calculus of the idea immanent in  
714 neural nets." *Bull. of Mathematical Biophys.*, 5: 115–133.

715           Moeinifard, P., M. S. Rajabi, and M. Bitaraf. 2022. "Lost vibration test data recovery  
716 using convolutional neural network: a case study." *arXiv Prepr. arXiv2204.05440*.

717           Murphy, G., D. Igoe, P. Doherty, and K. Gavin. 2018. "3D FEM approach for laterally  
718 loaded monopile design." *Comput. Geotech.*, 100: 76–83.  
719 [HTTPS://DOI.ORG/10.1016/J.COMP GEO.2018.03.013](https://doi.org/10.1016/j.compgeo.2018.03.013).

720           Nguyen, Q. H., H.-B. Ly, L. S. Ho, N. Al-Ansari, H. Van Le, V. Q. Tran, I. Prakash,  
721 and B. T. Pham. 2021. "Influence of data splitting on performance of machine learning models  
722 in prediction of shear strength of soil." *Math. Probl. Eng.*, 2021: 1–15. Hindawi Limited.

723           Patterson, J., and A. Gibson. 2017. *Deep learning: A practitioner's approach*. "O'Reilly  
724 Media, Inc."

725           Peng, J.-R., M. Rouainia, and B. G. Clarke. 2010. "Finite element analysis of laterally  
726 loaded fin piles." *Comput. Struct.*, 88 (21): 1239–1247.  
727 <https://doi.org/10.1016/j.compstruc.2010.07.002>.

728           Pham, T. A., V. Q. Tran, H. L. T. Vu, and H. B. Ly. 2020. "Design deep neural network  
729 architecture using a genetic algorithm for estimation of pile bearing capacity." *PLoS One*, 15  
730 (12): e0243030. Public Library of Science.

731           Sakleshpur, V. A., M. Prezzi, R. Salgado, and M. Zaheer. 2022. *CPT-Based  
732 Geotechnical Design Manual, Volume 2: CPT-Based Design of Foundations—Methods*.  
733 Purdue University.

734           Salgado, R., & Prezzi, M. (2007). Computation of cavity expansion pressure and  
735 penetration resistance in sands. *International Journal of Geomechanics*, 7(4), 251-265.



736           Shahin, M. A. 2016. “State-of-the-art review of some artificial intelligence applications  
737 in pile foundations.” *Geosci. Front.*, 7 (1): 33–44. Elsevier.

738           Spill, S., M. Kohlmeier, M. Wefer, S. Maretzki, and J. Dührkop. 2017. “Design of  
739 large-scale tests investigating the lateral load-bearing behavior of monopiles.” *Proc. Int.*  
740 *Offshore Polar Eng. Conf.*, 579–586.

741           Suryasentana, S. K., and B. M. Lehane. 2016. “Updated CPT-based p–y formulation  
742 for laterally loaded piles in cohesionless soil under static loading.” *Geotechnique*, 66 (6):  
743 445–453. ICE Publishing.

744           Taborda, D. M. G., L. Zdravkovic, D. M. Potts, H. J. Burd, B. W. Byrne, K. G. Gavin,  
745 G. T. Houlsby, R. J. Jardine, T. Liu, C. M. Martin, and R. A. McAdam. 2020. “Finite-element  
746 modelling of laterally loaded piles in a dense marine sand at Dunkirk.” *Geotechnique*, 70  
747 (11): 1014–1029. <https://doi.org/10.1680/jgeot.18.PISA.006>.

748           Tan, C., F. Sun, T. Kong, W. Zhang, C. Yang, and C. Liu. 2018. “A Survey on Deep  
749 Transfer Learning.” *Artif. Neural Netw. Mach. Learn. – ICANN 2018, Lecture Notes in*  
750 *Computer Science*, V. Kůrková, Y. Manolopoulos, B. Hammer, L. Iliadis, and I.  
751 Maglogiannis, eds., 270–279. Cham: Springer International Publishing.

752           Wakai, A., S. Gose, and K. Ugai. 1999. “3-D Elasto-Plastic Finite Element Analyses  
753 of Pile Foundations Subjected to Lateral Loading.” *Soils Found.*, 39 (1): 97–111.  
754 <https://doi.org/10.3208/sandf.39.97>.

755           Xu, Y., and R. Goodacre. 2018. “On splitting training and validation set: a  
756 comparative study of cross-validation, bootstrap and systematic sampling for estimating the  
757 generalization performance of supervised learning.” *J. Anal. Test.*, 2 (3): 249–262. Springer.

758 Xiao, T., L. M. Zhang, R. W. M. Cheung, and S. Lacasse. 2022. “Predicting spatio-  
759 temporal man-made slope failures induced by rainfall in Hong Kong using machine learning  
760 techniques.” *Geotechnique*.

761 Xu, L.-Y., F. Cai, G.-X. Wang, and K. Ugai. 2013. “Nonlinear analysis of laterally  
762 loaded single piles in sand using modified strain wedge model.” *Comput. Geotech.*, 51: 60–71.  
763 Elsevier Ltd.

764 Zhang, J. Z., D. M. Zhang, H. W. Huang, K. K. Phoon, C. Tang, and G. Li. 2022.  
765 “Hybrid machine learning model with random field and limited CPT data to quantify horizontal  
766 scale of fluctuation of soil spatial variability.” *Acta Geotech.*, 17 (4): 1129–1145. Springer  
767 Berlin Heidelberg.

768

769 **8 APPENDIX**

770 Table 2- Parameters and their ranges for the training data; i represents the layer number (3  
771 layers of sand). SI units are used for parameters

Parameter	Symbol	Parameter value, distribution, or formula
Pile diameter (m)	B	~ Uniform (2, 8)
Pile length (m)	L	= $3B + 12B \times \text{Uniform}(0,1)$
Wall thickness ratio	B/t <sub>w</sub>	~ Uniform (40, 100)
Inner diameter (m)	ID	= B - 2 × wall thickness
Area moment of inertia (m <sup>4</sup> )	I <sub>p</sub>	= $\pi \times (B^4 - ID^4) / 64$
Load eccentricity (m)	h	~ Uniform (15, 30)
Thickness of layer 1 (m)	t <sub>1</sub>	= $0.5B + (L-0.5B) \times \text{Uniform}(0,1)$
Thickness of layer 2 (m)	t <sub>2</sub>	= $(L - t_1) \times \text{Uniform}(0,1)$
Thickness of layer 3 (m)	t <sub>3</sub>	Total soil domain thickness-t <sub>1</sub> -t <sub>2</sub>
Relative density (%)	D <sub>R</sub>	~ Uniform (35, 90)
Effective unit weight (kN/m <sup>3</sup> )	γ'	= $(G_s-1)\gamma_w/(1 + e)$
Vertical effective stress, calculated each 0.2 m in depth (kPa)	σ' <sub>v</sub>	Calculated cumulatively from γ'
Horizontal effective stress, calculated each 0.2 m in depth (kPa)	σ' <sub>h</sub>	= $K_0 \times \sigma'_v$
CPT cone resistance (MPa)	q <sub>c</sub>	Calculated using Eq. 1

772

773